Journal of The Electrochemical Society, **154** (9) B910-B918 (2007)
0013-4651/2007/154(9)/B910/9/$20.00 © The Electrochemical Society

Measurement of Temperature and Reaction Species in the Cathode Diffusion Layer of a Free-Convection Fuel Cell

Tibor Fabian,[a,z] Ryan O'Hayre,[b,*] Fritz B. Prinz,[a,c,*] and Juan G. Santiago[a]

[a]*Department of Mechanical Engineering, Stanford University, Stanford, California 94305, USA*
[b]*Department of Metallurgical and Materials Engineering, Colorado School of Mines, Golden, Colorado 80401, USA*
[c]*Department of Material Science and Engineering, Stanford University, Stanford, California 94305, USA*

Micron- and millimeter-scale sensors were employed to acquire first-of-their-kind experimental measurements of the spatial and temporal distributions of temperature, oxygen partial pressure, and relative humidity in the mass transport layer immediately above the planar, horizontal cathode of polymer electrolyte membrane fuel cell (PEMFC) driven by natural convection. The sensors provide approximately 1 mm (or better) spatial resolution and 1 s temporal resolution. Substantial changes in temperature and reaction species concentrations were observed with increasing current density during a current-voltage (*I–V*) scan. A linear decrease in oxygen partial pressure and a linear increase in water vapor partial pressure were observed with increasing current density, consistent with a flux balance analysis. Spatially resolved profiles normal to the surface indicate that thermal and reaction species gradients extend up to 6 mm above the horizontal cathode surface. Complementary horizontal profiles (parallel to the surface) reveal that the cell's cathode rib structure visibly influences oxygen distribution. Most significantly, these data show that thermal and species concentration effects are not confined to the gas diffusion layer (GDL), but extend well beyond the cathode surface, into the surrounding space. The measurements were used to estimate diffusion and/or convection mass transfer coefficients above the cathode surface. Transient data reveal substantial differences in the time constants associated with oxygen, water, and heat transport. The insights provided by this study should prove useful to inform and validate future physical models of air-breathing fuel cell systems.
 [DOI: 10.1149/1.2752971]

Manuscript submitted January 12, 2007; revised manuscript received May 1, 2007. Available electronically July 10, 2007.

Passive air breathing fuel cells rely on natural convection to deliver oxidant and remove water and heat from the cathode surface. During operation, heat and water production and oxygen consumption give rise to temperature and concentration gradients above the cathode surface. These gradients induce changes in air density, thus driving the natural convection process. Although these coupled mass and heat transfer processes play a crucial role in determining performance, they have not been studied carefully in the context of passive air breathing fuel cell systems.

Nonuniform temperature and concentration effects have been studied to some extent in the context of forced-flow fuel cells using a variety of in situ probing techniques. For example, several groups have recently reported progress on monitoring spatial and/or temporal variations in temperature and species distributions in forced-flow single cells and stacks. Mench et al.[1] employed a multi-ported, segmented, serpentine cell interfaced to a gas chromatograph (GC) that allowed in-situ spatial and temporal determination of temperature, water vapor, nitrogen, oxygen, and current density distributions during fuel cell operation. The time resolution of their system was limited by the 2 min analysis time of the GC, while the spatial resolution was limited by the spacing of the species extraction ports, located in fixed positions approximately 1.2 cm apart. More recently, a Department of Energy project group including T. J. McIntyre of Oak Ridge National Laboratory[1] developed free-space microprobes and monolithically integrated fiber optic sensors to monitor spatial and temporal distributions of temperature and species within an operating fuel cell stack. Because water dynamics are of particular importance in most polymer electrolyte membrane fuel cell (PEMFC) designs, considerable effort has also been directed towards neutron imaging,[2-4] magnetic resonance imaging,[5,6] and optically transparent cells[7,8] to image the in situ production and distribution of water in operating PEMFCs. In contrast to forced-flow fuel cells, planar air-breathing fuel cells offer enviable access to the cathode surface. This open architecture provides a unique opportunity to acquire detailed, high-resolution information about free-convection mass transport processes in the vicinity of the cathode surface.

In this paper, we employ micro- and millimeter-scale temperature, oxygen, and humidity sensors to measure spatial and temporal distributions of temperature, oxygen partial pressure, and relative humidity (RH) in the mass transport layer immediately above the cathode of a natural-convection driven planar horizontal PEM fuel cell. Spatially resolved temperature and species profiles are obtained by mounting the cell on an optical XYZ translation stage. A spatial resolution of less than 1 mm is demonstrated; this is limited primarily by measurement uncertainty and the physical size of the microsensors. Time resolution on the order of seconds is easily achieved; and this is limited largely by the response time of the microsensors. These spatial and temporal measurements provide a first-of-their-kind experimental quantification of the diffusion layer thickness, time constants, and transfer coefficients of an air-breathing fuel cell cathode. The results yield insight into the processes governing the behavior of passive air breathing fuel cells, provide the basis for new diagnostic test procedures, and provide direction for future air breathing fuel cell design.

Experimental

In this section we present details of planar fuel cell design and the setup used to simultaneously record current, voltage, temperature, oxygen, and relative humidity data. We also describe the *Z* (vertical) and *Y* (horizontal) spatial profile scan procedures; the transient (temporal) measurement method; and the calibration methods required to temperature correct the oxygen and RH microsensor readings.

Cell hardware.— The fuel cell assembly employed in these studies has been described previously in detail elsewhere,[9] and is only summarized briefly here. The outer dimensions of the system are 7 by 7 by 1 cm. The hydrogen feed chamber is a Delrin, machined back plate with two hydrogen distribution channels (each 5 mm wide, 5 mm deep, and 3 cm long). We use a printed circuit board (PCB) anode structure with 1.5 mm wide parallel flow channels spaced 1.5 mm apart.[10,11] We use a self-humidifying, Nafion 112-based five-layer membrane electrode assembly (MEA) (BCS Fuel Cells Inc, Bryan, Texas) with 3 by 3 cm active area and 3 mg/cm^2 catalyst loading on the cathode and 0.5 mg/cm^2 on the anode. A 316L stainless steel sheet 150 μm thick coated with 10 mm Ni and 1 mm Au serves as the cathode current collector. The stainless sheet has an array of etched circular openings 150 μm in diameter that

* Electrochemical Society Active Member.
z E-mail: tibor.fabian@stanford.edu

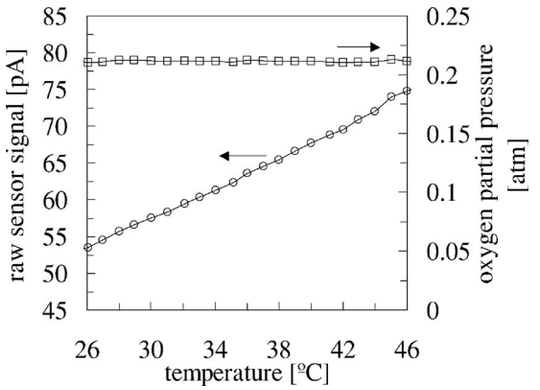

Figure 1. Plot of oxygen microsensor current output and temperature-calibrated oxygen concentration as a function of air temperature.

facilitate water and oxygen transport through the current collector. The top layer of the cathode is a rigid PCB superstructure with 11 parallel ribs 1.5 mm wide and 1.5 mm apart (3 mm center to center distance). We deposited 66 μm of Cu, 10 μm Ni, and 1 μm Au on the PCB superstructure to improve conductance and inhibit corrosion.[12] Eight bolts hold the assembly together and the torque on each bolt was 1 Nm. Silicone rubber gaskets placed between individual layers seal the anode compartment and provide for optimal MEA compression.

Oxygen microsensor.— The partial pressure of oxygen was measured with a miniature Clark-type electrochemical sensor (Unisense OX25, ~25 μm capillary tip radius) consisting of three electrodes embedded in a tubular glass body with a thin capillary at one end. The sensor electrodes were connected to a current amplifier (Unisense, PA2000 picoammeter) that converted the picoamp-level sensor current to a dc voltage.

The sensor readout was temperature corrected due to the strong temperature dependence of the sensor current. The temperature was measured with an unsheathed fine gauge *K*-type thermocouple (CHAL-005, Omega Engineering, Inc., ~125 μm diameter) collocated in the vicinity of the capillary probe. The temperature compensation procedure assumed that the temperature measured by the thermocouple was identical to the temperature experienced by the oxygen probe. Given the small size and close proximity of the two probes (less than half a mm center to center), this assumption was very reasonable for most of the thermal gradient conditions presented here.

Clark-type electrochemical oxygen sensors measure the current produced by the electrochemical reduction of oxygen diffusing through a thin, oxygen-selective membrane.[13] Because the sensor is operated under oxygen diffusion limitation, output signal increases linearly with increasing oxygen concentration. However, because diffusion is a temperature-activated process, the signal increases exponentially with increasing temperature.[14] In general, the signal S produced by the sensor may be described as follows:[15]

$$S(P_{O_2},T) = Z + P_{O_2}Ae^{kT} \quad [1]$$

where P_{O_2} is the partial pressure of oxygen, T is sensor tip temperature, Z is the sensor current at zero oxygen partial pressure, and A and k are fitting constants that describe the temperature dependence of the sensor. The zero current, Z, can be extracted by exposing the sensor to a zero-oxygen environment (for example, by exposure to a pure nitrogen atmosphere). The fitting constants A and k were then determined from a series of temperature measurements at known P_{O_2}. This temperature correction procedure was robust and reliable across the experimentally investigated temperature range. For example, Fig. 1 presents the raw and calibrated, temperature corrected data acquired from an oxygen sensor in air ($P_{O_2} = 0.21$) heated from room temperature to 46°C. The tip of the oxygen microsensor was placed less than a millimeter above the surface of a hot plate. The temperature of the tip was incrementally increased by adjusting the temperature of the hot plate. The temperature of the oxygen microsensor tip was measured with a miniature thermocouple placed in the close vicinity of the sensor tip. Radiative heat transfer to the thermocouple was minimized with a low emissivity hot-plate surface (aluminum foil). Although the raw sensor signal increases from 52 to 75 pA upon heating, the temperature corrected P_{O_2} value remains steady at ~0.21 atm (the expected value for air). The calibration values used in this case were $Z = 1.0$, $A = 1.67$ and $k = 0.0167$. To ensure accurate results, the oxygen sensor was temperature calibrated before and after each experimental run. Calibration parameters typically drifted only slightly (less than 10% maximum, and typically less than 5%) with time.

Humidity sensor.— The relative humidity was measured with a fiber-optic sensor system consisting of a 1550 nm axial Bragg-grating fiber-optic strain sensor (GACS0-01FP0100, Blue Road Research), optical beam splitter (BS3DB, Blue Road Research), 1550 nm broadband light source (HP 83437A, Hewlett-Packard), and an optical spectrum analyzer (AQ6317B, Ando). The fiber-optic sensor was formed by an optical fiber with a polymer coated Bragg grating at the end of the fiber. The diameter of the coated fiber was about 150 μm, and the grating was approximately 3 mm long. The 1550 nm wideband light source was optically connected to one port of the beam splitter. The transmitted light from the beam splitter was fed into the fiber with the Bragg grating. The light reflected from the humidity probe was analyzed with the optical spectrum analyzer at the output of the beam splitter. The relative humidity reading was determined from the center wavelength of the signal spectrum reflected by the Bragg grating. The center wavelength was determined with picometer resolution by curve fitting the grating response to a predefined filter response.

The Blue Road Research Bragg-grating fiber-optic humidity sensor utilizes a strain-based method to measure relative humidity.[16] A fiber-optic Bragg grating behaves like a narrow-band notch filter. It reflects light in a narrow bandwidth determined by the total length of the grating with a center frequency determined by the spacing between the gratings. Thus, by monitoring the center wavelength of the reflected signal, elastic strain-induced changes in the grating spacing can be precisely tracked. The fiber was coated with a moisture sensitive polyamide film that responds linearly to changes in relative humidity. (The film swells with increasing relative humidity, inducing tensile strain in the fiber grating.) However, the probe also responds linearly to temperature, due to the thermal expansion properties of the glass fiber. Temperature calibration is therefore required to extract the portion of the probe signal that is due only to changes in relative humidity. As an approximation, the center wavelength of the Bragg grating filter response can be modeled as linearly dependent on temperature and relative humidity[16]

$$\lambda(\mathrm{RH},T) = \lambda_0 + k_{\mathrm{RH}}\mathrm{RH} + k_{\mathrm{T}}T \quad [2]$$

where λ_0, k_{RH}, and k_{T} must be determined by calibration. During the calibration procedure, the humidity sensor and a reference humidity sensor (SHT11, Sensirion, Westlake Village, CA) were placed inside an environmental chamber (SM-3.5S, Thermotron, Holland, MI). The chamber was then programmed to vary relative humidity between 40 and 80% RH at 20, 30 and 40°C. The temperature and the relative humidity of the reference sensor, the center wavelength of the light reflected by the Bragg grating, and the probe temperature were sampled periodically. The calibration constants were then obtained by a fit of the relative humidity obtained by the reference sensor to values calculated with the filter center wavelength. Figure 2 shows the time-varying relative humidity and temperature readings of the reference sensor as well as the temperature-corrected relative humidity readings of the fiber-optic humidity probe during a typical calibration. Humidity was cycled from 40 to 70% every 240 min while temperature was varied from 20 to 40°C over

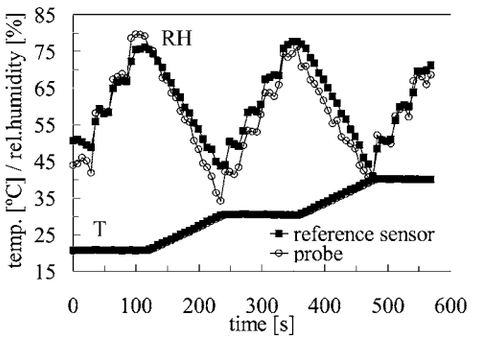

Figure 2. Comparison of relative humidity measurements by the microprobe used here and a reference sensor as a function of humidity and temperature.

540 min. The probe agrees well with the reference sensor, confirming that relative humidity measurements were corrected for temperature. The typical values for λ_o, k_{RH}, and k_T were 1500 nm, ~1 pm/%RH, and ~10 pm/°C. The time response of the sensor was limited by the sampling and averaging necessary to obtain pm resolution of the center wavelength measurement. After calibration our estimated absolute accuracy of the relative humidity readout was approximately ±12%RH.

In discussing water vapor transport under nonisothermal conditions, we find helpful converting relative humidity data into partial water vapor pressure (P_{H_2O}) data. While relative humidity reflects the activity of water vapor at a particular temperature, P_{H_2O} reflects the actual concentration (pressure) of water at that temperature. (To highlight the important difference between RH and P_{H_2O}, consider that air at 80°C and 20% RH contains far more water, P_{H_2O} ~ 0.10 atm, than air at 10°C and 80% RH where P_{H_2O} ~ 0.01 atm.) To convert between RH and P_{H_2O} data in this paper, we used the following standard polynomial expression for the saturation pressure of water[17]

$$P_{H_2O} = \frac{RH}{100} 10^{(-2.1794+0.02953T-9.1837\times10^{-5}T^2+1.4454\times10^{-7}T^3)} \quad [3]$$

where P_{H_2O} is the water vapor partial pressure (atm), RH is the relative humidity (%), and T is the temperature (°C).

Experimental setup.— Figure 3a illustrates schematically the configuration for the air-breathing fuel cell cathode microsensor probing experiments. The planar air-breathing fuel cell was attached on top of a XYZ micromanipulation stage with the open cathode facing upwards. The cell was thermally insulated from the XYZ stage with an insulation layer and convectively shielded from the environment by an enclosure. The temperature, oxygen partial pressure, and relative humidity sensors were mounted on rigid optical posts, which were in turn fixed to a rigid optical breadboard. All three sensors were aligned so that they converged on a small volume of space in a region above the central part of the cathode of the air-breathing fuel cell. The relative placement of the sensors is shown in magnified detail in Fig. 3b. The air-breathing fuel cell was placed on an optical XYZ stage attached to the same optical breadboard base, ensuring a robust, mechanically complete, rigid assembly. The XYZ stage allowed for precision control of displacement between the cathode surface and the sensors. The Clark capillary sensor and the fiber-optic Bragg sensor were arranged in collinear fashion with less than a millimeter spacing between the tips of the sensors. The thermocouple wires were routed in air in parallel with and above the optical fiber. The actual thermocouple was located at the start of the Bragg grating less then a half millimeter above the optical fiber. The entire experimental setup was sheltered inside a

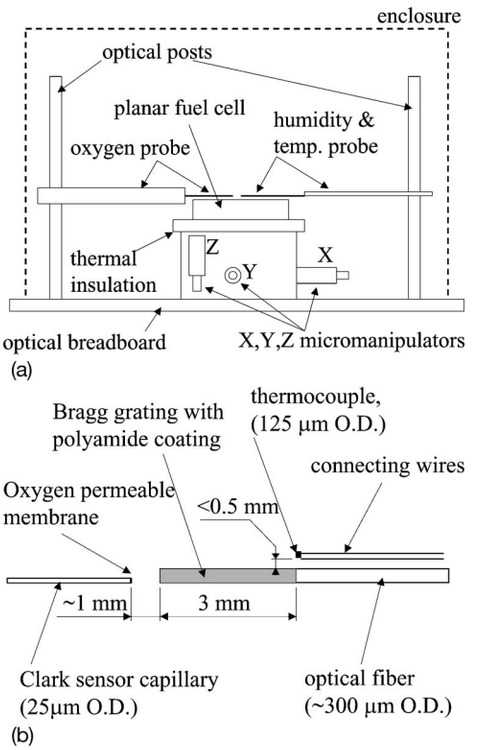

Figure 3. (a) Schematic diagram of the experimental setup, (b) schematic side view of the probe assembly.

partial enclosure structure to minimize the effects of forced flows occurring in the laboratory environment on the natural convection plume above the fuel cell cathode.

The relative location of the planar cathode and the sensor assembly during polarization, profile, and transient measurements is detailed in Fig. 4. The sensor assembly consists of oxygen sensor capillary, the optical fiber with humidity sensitive Bragg grating, and the thermocouple with wires. The sensors were always arranged in parallel with each other and with the cathode ribs. The arrangement of the sensors relative to each other remained fixed during all experiments. The geometric points A (y = 0 mm, z = 0 mm), B (y = 0 mm, z = ~ 6 mm), C (y = −1.52 mm, z = ~ 0.16 mm), D (y = 1.52 mm, z = 0.16 mm), and E (y = 0 mm, z = 1.6 mm) define the trajectories and the locations of the sensor assembly (referenced by the geometric center of the Bragg grating) during experiments (x = 0 mm for all experiments). Lines EB, and CD represent the loci of sensor assembly during z (vertical) and y (horizontal) traverses, respectively. The relative humidity z traverse was measured with a modified sensor assembly along the AB line. During polarization and transient scans the sensor assembly was located at point E. The center of the coordinate system was located in the geometric center of the cathode active area with the optical fiber touching the top of the cathode mesh.

Measurement procedure.— A new MEA experiences a "break in" period where the resistance gradually decreases during use.[18] We avoid initial transient effects by conditioning each new membrane in the cell for 10 h at 0.5 V at ambient temperature and humidity. Furthermore, we conditioned the fuel cell prior to each experiment. First, we removed any condensed water by purging the anode compartment and cathode surface with dry compressed air. Next, we purged the anode compartment with hydrogen and sealed off the anode. Before each experiment, we operated the cell at 900 mA (100 mA/cm^2) constant current for 15 min.

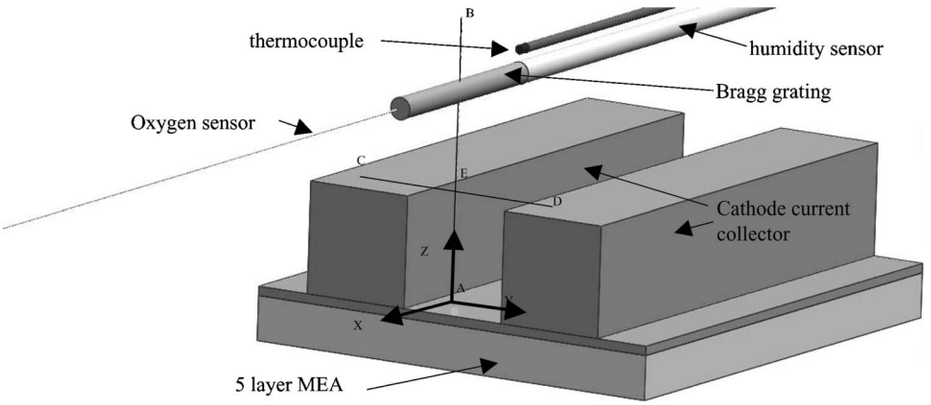

Figure 4. Schematic diagram of relative arrangement of sensors and fuel cell cathode during polarization, profile, and transient measurements.

Polarization scans.— For these, the sensor assembly was located at $z = \sim 1.6$ mm, $y = 0$ mm (in the middle of the channel, flush with the top of the cathode ribs), see location E in Fig. 4. Current-voltage polarization scans (*I–V* curves) were acquired by increasing the fuel cell current in 450 mA steps (50 mA/cm^2) in 5 min intervals until the cell voltage dropped below a 0.4 V threshold level. Temperature, relative humidity, and oxygen partial pressure were continuously tracked by the microsensor assembly. After each current step, we allowed the fuel cell voltage to stabilize over the 5 min period and then recorded the ending period cell potential, temperature, relative humidity, and P_{O_2}. Relative humidity readings were subsequently converted to P_{H_2O} values based on the measured temperature using Eq. 3.

Profile scans.— Spatially resolved concentration and temperature profiles were extracted by translating the fuel cell underneath the fixed microsensor assembly. During the horizontal *y* traverse, the location of the sensor assembly relative to cathode was incrementally changed from point C at $z = 1.6$ mm and $y = -1.5$ mm (the center of a first cathode rib flush with the top cathode rib surface; point C) to point D at $z = 1.6$ mm, and $y = 1.5$ mm (the center of an adjacent cathode rib flush with the top cathode rib surface). See also Fig. 4.

The partial pressure of oxygen and humidity were measured in separate vertical *z* traverse. During relative humidity *z* traverse the location of sensor assembly relative to cathode surface was incrementally changed from starting point at $z = 1.5$ mm and $y = 0$ mm (the center of cathode channel, flush with top of the cathode ribs), see also point E in Fig. 4, to an end point at $z = 6$ mm, $y = 0$ mm (the center of cathode channel, 6 mm above the cathode surface), see also point B in Fig. 4. The small measurement volume of the oxygen probe and thermocouple allowed for P_{O_2} measurements starting from the bottom of the channel. The oxygen partial pressure *z* traverse was measured with a modified sensor assembly. The optical fiber with the Bragg grating was removed from the sensor assembly and the thermocouple was brought into the vicinity of the oxygen permeable membrane of the Clark sensor. Further, both sensors were tilted downwards. This tilt allowed us to have the sensor tips approach the bottom of the cathode channel without touching the rest of the cathode.

For all profile scans, the minimum translation step size used was 10 mil (254 μm). After each translation step, the cell was allowed to re-equilibrate for a period of 2 min before temperature, relative humidity, and P_{O_2} readings were recorded.

Transient measurements.— Transient effects were studied using a current interrupt technique. The fuel cell was first conditioned for 30 min at the current density of interest to attain a stable operating condition. The current was then abruptly zeroed, and the transient response of the fuel cell voltage, microsensor temperature, partial oxygen pressure, and relative humidity were recorded. During these transient measurements, the microsensor assembly was positioned at $y = 0$ mm, $z = 1.6$ mm (approximately in the middle of the fuel cell cathode, flush with the top of the channel ribs, and approximately centered within the middle of a channel), see point E in Fig. 4.

Intrinsic sensor response speed was quantified to determine if the temperature, partial oxygen pressure, and relative humidity probes were sufficiently fast compared to the speed of the observed transient fuel cell phenomena. Intrinsic sensor response speed was measured by subjecting each sensor to fast change in stimulus. The results of this analysis are provided in Fig. 5a and Fig. 5b. The thermocouple was subjected to an abrupt change in temperature from 29° to 21°C by first placing it above the surface of a hot plate and then rapidly removing it from above the hot plate. The oxygen sensor was subjected to an abrupt change in P_{O_2} at constant temperature from 0.21 to 0 atm by first encapsulating the sensor in a small volume enclosure filled with ambient air and then displacing the air in the enclosure with a jet of argon. The relative humidity sensor was subjected to an abrupt change in RH from 80 to 45% (at constant temperature) by first placing the sensor to environmental chamber set to same temperature as ambient but higher humidity than ambient and then removing the humidity sensor from the envi-

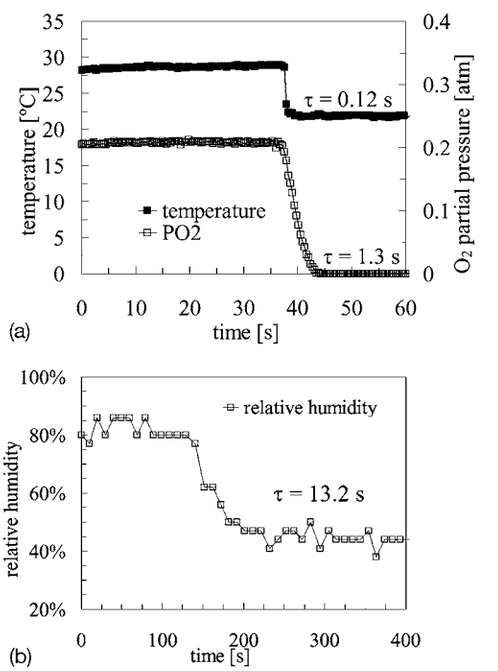

Figure 5. (a) Transient response of the temperature and P_{O_2} microsensors, (b) transient response of the relative humidity microsensor.

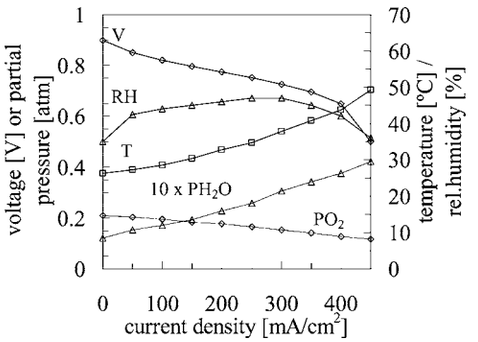

Figure 6. Measurements of voltage, temperature, RH, P_{O_2}, and P_{H_2O} as a function of current density for the planar air-breathing fuel cell during a standard polarization scan.

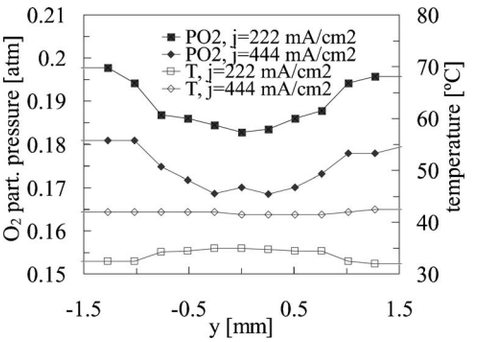

Figure 7. Measurements of temperature and partial oxygen pressure, P_{O_2}, as a function of sensor assembly location during a y traverse at $z = 1.6$ mm from $y = -1.52$ to $y = 1.52$ mm for two current density loads of 222 and 444 mA/cm^2.

ronmental chamber to ambient environment. We approximate the time constants of these induced changes as, respectively, <0.01 s, <0.1 s, and <2 s. The speed of the sensor response was quantified by fitting the transient signal rise time to a single exponential function, yielding a response time constant τ for each sensor. This analysis provided $\tau_{\text{thermocouple}} = 0.12$ s, $\tau_{O_2\ \text{sensor}} = 1.3$ s, and $\tau_{\text{RH sensor}} = 13$ s, respectively. This analysis indicated that the thermocouple was sufficiently fast to investigate the transient fuel cell phenomena discussed in this paper (see Fig. 11). However, the P_{O_2} and RH sensor speeds were in some cases comparable to the observed fuel cell P_{O_2} and RH transients, making quantitative analysis of these transient data difficult. The P_{O_2} sensor speed was limited primarily by the speed of oxygen diffusion through the oxygen selective sensor membrane, while the RH sensor speed was limited primarily by the (real time) averaging and curve fitting required for pm center wavelength resolution.

Results and Discussion

In this section we first present simultaneous *I–V*, temperature, P_{O_2}, RH, and P_{H_2O} data acquired during a polarization scan of the air-breathing fuel cell. We then show temperature, P_{O_2}, and RH profiles acquired from vertical z and horizontal y traverses of the cathode surface under fixed current load conditions. Finally, we discuss the transient responses observed for voltage, temperature, P_{O_2}, and RH induced by an abrupt current interrupt cycle.

Current-voltage polarization.— Figure 6 presents the *I–V* polarization scan of the air-breathing fuel cell with simultaneous measurements of temperature, P_{O_2}, RH, and P_{H_2O} response for the microsensor unit positioned above the fuel cell cathode surface ($y = 0$ mm, $z = 1.6$ mm). Ambient laboratory conditions during measurement were $T_{\text{ambient}} = 21°\text{C}$, $\text{RH}_{\text{ambient}} = 44\%$. With increasing current density, the microsensors recorded significant thermal heating, oxygen depletion, and water production in the vicinity of the cathode surface. Although most of the trends in Fig. 6 make intuitive sense, the RH response deserves some discussion. RH initially climbs slightly with increasing current density, and then has a slight drop at the highest current densities. These trends in RH are best understood when coupled with temperature readings and converted into P_{H_2O} values. As shown in the figure, P_{H_2O} increases linearly with increasing current. The near-surface RH is an indication of the ohmic performance of the membrane, while the P_{H_2O} values describe the net rate of mass transport from the cathode. At high current density, there is increased P_{H_2O} (indicating increased reaction rates), but the higher temperature implies a drop in RH (saturation water vapor pressure increases exponentially with temperature), see Eq. 3 above. The latter leads to a significant increase in membrane resistance and hence a decline in cell potential. This is particularly true for current densities above about 350 mA/cm^2, where temperature effects on RH dominate and cell potential drops steeply. These trends in P_{H_2O} and RH vs current density are captured by our air-breathing fuel cell model.[19]

The fact that P_{O_2} decreases linearly with increasing current density, while P_{H_2O} increases linearly with increasing current density, is expected based on the linear correspondence between current density and reactant consumption (or product creation). Assuming that the sensor probes are located within the diffusion layer, a simple flux balance yields the following linear relationship:

$$j = -nFkD^{\text{eff}}\frac{\Delta c}{\delta} \qquad [4]$$

Here j is the current density, n is the reaction number, F is Faraday's constant, D^{eff} is the effective diffusivity, Δc is the change in concentration across the diffusion layer, δ is the characteristic diffusion layer thickness, and k is the fraction of active area not blocked by cathode current collectors. Extraction of further details about the cathode diffusion layer is difficult based on Fig. 6 alone. However, further details of the process (including estimates of D^{eff} and δ) can be obtained by analyzing spatial variations and transient responses as discussed below.

Profile (Z and Y) scans.— Figure 7 shows measured temperature and P_{O_2} profiles extracted from y-traverse (horizontal) measurements across the fuel cell cathode surface at $z = 1.6$ mm from $y = -1.52$ to 1.52 mm in 254 μm increments and operating current densities of 222 and 444 mA/cm^2. Figure 8 provides RH and P_{H_2O} profiles extracted from a second set of y traverse at $z = 1.6$ mm

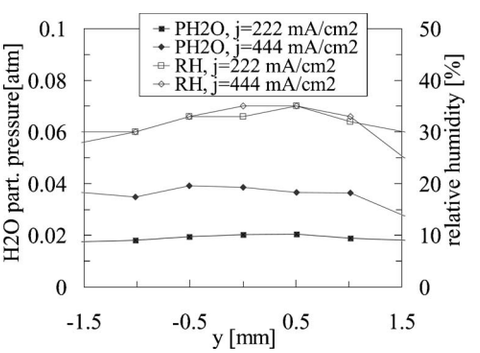

Figure 8. Measurements of water vapor partial pressure, P_{H_2O}, and relative humidity, RH, as a function of sensor assembly location during a y traverse at $z = 1.6$ mm from $y = -1.52$ mm to $y = 1.52$ mm for two current density loads of 222 and 444 mA/cm^2.

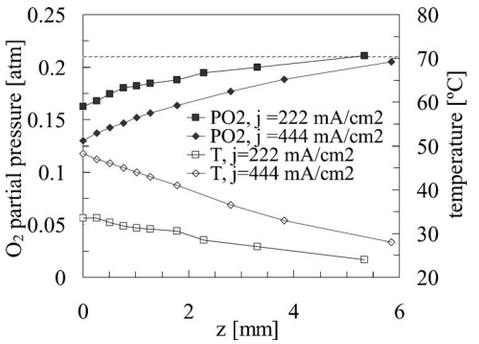

Figure 9. Measurements of partial oxygen pressure and temperature as a function of sensor assembly location during a z traverse from $z = 0$ mm to $z = 6$ mm at $y = 0$ mm for two current density loads of 222 and 444 mA/cm^2. The dotted line shows the ambient oxygen concentration.

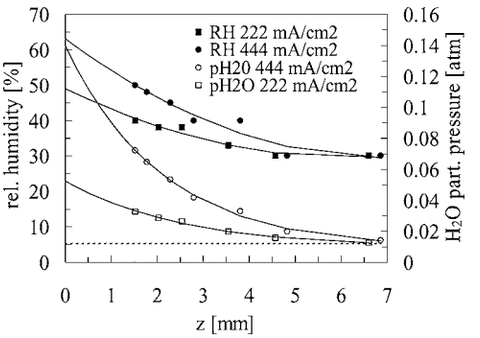

Figure 10. Measurements of relative humidity and partial water vapor pressure as a function of sensor assembly during a z traverse from $z = 1.5$ mm up to $z = 7$ mm for two current density loads of 222 and 444 mA/cm^2. The recorded relative humidity and temperature (not shown) readouts (filled markers) were approximated with a second order polynomial fit (solid line) and extrapolated to $z = 0$. The water vapor concentrations determined from actual measured values are shown with empty markers while the solid line shows water vapor concentration obtained from the approximations of temperature and relative humidity with second order polynomials. The dotted line shows the ambient water vapor concentration during the experiment (21°C and 45% relative humidity).

from $y = -1.52$ to 1.52 mm in 508 μm increments, and the same operating points. The P_{O_2} profiles show a strong effect due to the channel ribs, while the RH and P_{H_2O} profiles are less influenced by the ribs. The temperature profiles are nearly independent of the position of the ribs most probably due to the high thermal conductivity of the ribs. From these measurements we can deduce the relative dimensions of the oxygen, water vapor, and temperature diffusion layers. We hypothesize that scalar fields strongly influenced by the location of the ribs indicate smaller diffusion layers with characteristic lengths comparable or smaller than the characteristic dimensions of the ribs.

As expected, the higher current density operation point leads to higher temperature, greater oxygen depletion, and increased water output (as illustrated by a maximum in the temperature curve, a minimum in the P_{O_2} curve, and a maximum in the P_{H_2O} curve for $j = 444$ mA/cm^2). At the same time, the higher current density operation point leads to decrease in relative variations of P_{O_2}, P_{H_2O}, and temperature as a function of y. These trends are consistent with an increase of the diffusion layer thickness with increasing current density. Interestingly there is very little variation of RH with changing current density. Larger current density increases local product water vapor, but is accompanied by larger temperatures so that RH is approximately unchanged.

Figure 9 provides temperature and P_{O_2} profiles extracted from z-traverse measurements starting from the bottom of a fuel cell cathode channel at the same two operating current densities. Figure 10 provides RH and P_{H_2O} profiles extracted from a second set of z-traverse at the same operating points but starting from the plane of the top cathode rib surface ($z = 1.5$ mm). Temperature, P_{O_2}, RH, and P_{H_2O} all show strong dependence on z location. Intriguingly, they all show long-range behavior, with gradients extending several millimeters above the cathode surface. We quantified the extent of the diffused layer by distance $\delta_{95\%}$ (in z direction) at which the difference between the local and ambient value of a measured species or temperature drops to 5% of its initial value at $z = 0$. The estimates of the diffused layer thickness at 222 and 444 mA/cm^2 were 4.5 and 5.4 mm for water vapor partial pressure, 4.3 and 6.1 mm for oxygen partial pressure, and 7.4 and 9.4 mm for temperature. These profiles suggest that the mass-transport diffusion layer at the air-breathing fuel cell cathode may have a significantly greater spatial extent than previously assumed.[20,21] We emphasize that special care was taken in these experiments to shield the fuel cell as much as possible from external convective air currents (in order to characterize the contribution of natural convection to the mass transfer, reduce sensor noise, and improve reproducibility). Air streams in enclosed rooms can show velocity values that are higher than natural convection induced air-flow streams (9–11 cm/s[9]) above planar air-breathing fuel cell cathode. These experimental conditions therefore likely represent a "worst-case" scenario of a controlled, quiescent ambient. Therefore, the y and z profiles presented here likely correspond to an upper bound limit for the size and influence of the diffusion layer. In realistic air-breathing fuel cell environments (e.g., in an office building), external convective currents will likely reduce the spatial extent of this diffusion layer.

The effective oxygen and water diffusion coefficients ($D^{\text{eff}}_{O_2}$ and $D^{\text{eff}}_{H_2O}$) at the fuel cell cathode surface/environment interface can be estimated based on the flux balance model of Eq. 4, as applied to the spatial O_2 and H_2O profiles measured in Fig. 9 and Fig. 10. Fitting the initial slope of these spatial profiles (from $z = 0$ to $z = 1$ mm), where a planar diffusion approximation is most likely to hold, yields $D^{\text{eff}}_{O_2}$ estimates of 0.14–0.26 cm^2/s and $D^{\text{eff}}_{H_2O}$ estimates of 0.21–0.38 cm^2/s. The estimates represent effective diffusivities that incorporate the effects of convection (if any) which would enhance mass transport. The $D^{\text{eff}}_{O_2}$ and $D^{\text{eff}}_{H_2O}$ values are on the order of published values for free diffusion coefficient of oxygen in air, D_{O2}, of 0.24–0.29 cm^2/s for 298 K $< T <$ 330 K and water vapor in air, D_{H_2O}, of 0.26–0.30 cm^2/s for 298 K $< T <$ 330 K.[22] The discrepancy between the measured and published values for the diffusivities may be due to effects of natural convection, nonplanar diffusion in the cathode channels, and uncertainties in the RH measurement due to finite volume of the humidity probe, differences between actual Bragg grating temperature and thermocouple readout, etc. As an alternate approach to the simple diffusion analysis presented above, we here present estimates of mass transfer coefficients. For this purpose, we describe convective-mass transfer using the following flux balance equation

$$j = -nF\bar{h}_{m,i}(c_{i,z=\infty} - c_{i,z=0}) \quad [5]$$

Here $\bar{h}_{m,i}$ is the average convection mass transfer coefficient of species i (cm/s), $c_{i,z=0}$ is the concentration of species i at $z = 0$, and $c_{i,z=\infty}$ is the ambient concentration of species i. The estimates of oxygen and water vapor mass transfer coefficients and values obtained during our previous modeling[19] are summarized in Table I.

The estimates for oxygen mass transfer are in line with our recent modeling results for similar load and ambient conditions of 20°C and 45% RH. The estimated water vapor mass transfer coefficient at the higher current density of 444 mA/cm^2 differs from the model prediction. We attribute this to measurement uncertainty of the water vapor concentration estimate, since the water vapor con-

Table I. Comparison between average water vapor and oxygen convective mass transfer coefficients obtained in this study with values obtained by a combined mass and heat transfer model (see Ref. 19) at current densities of 222 and 444 mA/cm^2.

		Estimated	Modeled (Ref. 19)
Species	Current density [mA/cm^2]	$\bar{h}_m$ [cm/s]	$\bar{h}_m$ [cm/s]
O_2	222	0.47	0.56
O_2	444	0.57	0.65
H_2O	222	0.59	0.66
H_2O	444	0.46	0.77

centration at the cathode surface was extrapolated from temperature and relative humidity values measured above the cathode ribs.

Unlike the mass flux, the heat flux from the cathode surface has to be treated as a sum of convective and radiative components as expressed in the following heat flux equation

$$q = h_T(T_{z=\infty} - T_{z=0}) \quad [6]$$

Here h_T is the total heat transfer coefficient and can be expressed as a sum of convective, h_{Tc}, radiative heat transfer coefficient, h_{Tr}. The radiative heat transfer coefficient is defined as

$$h_{Tr} = \varepsilon\sigma(T_{z=\infty}^2 + T_{z=0}^2)(T_{z=\infty} + T_{z=0}) \quad [7]$$

where ε is the surface emissivity, σ is the Boltzman constant, $T_{z=0}$ is the temperature at $z = 0$, and $T_{z=\infty}$ is the ambient temperature.

Table II compares estimates of convective and radiative average heat transfer coefficients obtained from temperature profiles shown in Fig. 9 with values obtained from our previous modeling.[19] We assumed that the cathode surface is gray, has emissivity of 0.9 and is isothermal. The fuel cell voltage used to calculate the generated heat was 0.75 V at a current load of 222 mA/cm^2 and 0.63 V at a current load of 444 mA/cm^2. The amount of heat generated at the fuel cell cathode depends not only on the fuel cell voltage and current but also on the fraction of product water that condenses and adds latent heat of condensation to the heat flux balance. Based on our previous experimental studies[9] we assumed that about 30% of product water condensed during our experiment. The estimated values are in good agreement with the values predicted by our modeling and differ by about 10%.

Transient measurements.— Figure 11a shows voltage, temperature, and P_{O_2} transients recorded during a current interrupt pulse cycle between 0 and 333 mA/cm^2. The voltage transient that occurs at approximately 375 s is difficult to resolve at the scale of Fig. 11a, and so a magnified version is provided in Fig. 11b. The oxygen transients in Fig. 11b can be fit to a single exponential model with a

Table II. Comparison of estimated and modeled (see Ref. 19) average heat transfer coefficients at two current density loads of 222 and 444 mA/cm^2. For all estimates we assumed that the cathode surface is isothermal, gray, and has a surface emissivity of 0.9. We also assumed that about 30% of generated water has condensed (see Ref. 9).

		Estimated	Modeled[a]
Heat transfer	Current density [mA/cm^2]	$\bar{h}$ [W/m^2 K]	$\bar{h}$ [W/m^2 K]
Radiative	222	5.9	5.6
Radiative	444	6.3	6.0
Convective	222	11.7	10.6
Convective	444	13.5	12.2

[a] Reference 19.

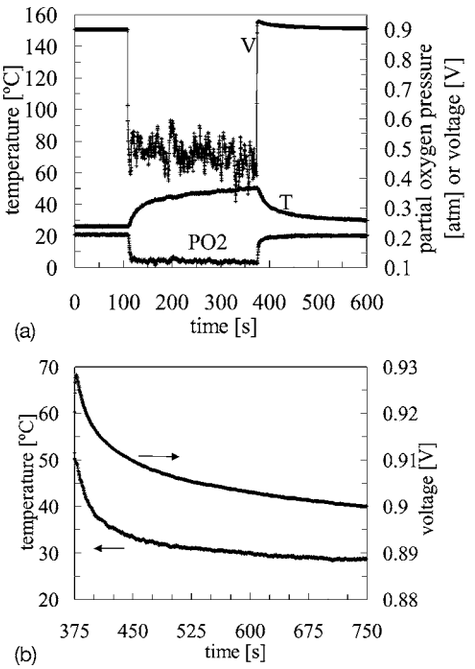

Figure 11. (a) Measurements of temperature, fuel cell voltage, and oxygen partial pressure as a function of time with sensor assembly located at $z = 0$ mm and $y = 0$ mm during a step current pulse between 0 and 333 mA/cm^2. (b) Detail of the temperature and voltage transients after the current transition at $t = 375$ s.

time constant $\tau_{O_2} \sim 6$ s. This short, single time constant is likely associated with O_2 diffusion in the boundary layer. In contrast, the temperature transients require a fit with both an exponential and a linear term. The exponential term ($\tau_T \sim 20$ s) is likely associated with the thermal mass of the fuel cell body as well as the buildup of the thermal boundary layer. The linear term ($\sim$0.19°C/min) is caused by continuous flooding of the cathode surface leading to mass transfer losses in the gas diffusion layer resulting in reduced cell potential, and increased heat generation. The linear term is absent if the liquid water is continuously removed from the cathode surface.[23]

Given the measured time-dependent recovery of the oxygen concentration, the effective oxygen diffusivity within the fuel cell cathode diffusion layer may be estimated using transient diffusion scaling arguments. To first order, diffusion transients follow the well-known scaling relationship

$$x = \sqrt{D^{eff}t} \quad [8]$$

where x is the characteristic length scale associated with the transient diffusion process, D^{eff} is the effective diffusivity, and t is the time. Using the diffusion-layer estimates obtained from our z-profile analysis ($x = \delta_{O_2} = 0.6$ cm) we can extract a rough estimate of the effective oxygen diffusivity from Eq. 8. This analysis yields $D_{O_2}^{eff} \sim 0.06$ cm^2/s. This estimate is similar, although slightly smaller than the value obtained from the previous flux balance analysis [Eq. 4 applied to the spatial O_2 profiles in Fig. 9]. We conclude that the transient technique likely slightly underestimates the real O_2 diffusivity due to the intrinsic sensor response limitation (see the section measurement procedure). The measured O_2 transient relaxation time ($t_{O_2} \sim 6$ s) is comparable to the intrinsic O_2 sensor speed ($t_{O_2\ sensor} \sim 1.3$ s), causing "instrument broadening" of the O_2 transient signal. Using a smaller capillary diameter O_2 microsensor would improve sensor speed, but at the expense of increased noise and decreased sensor stability.

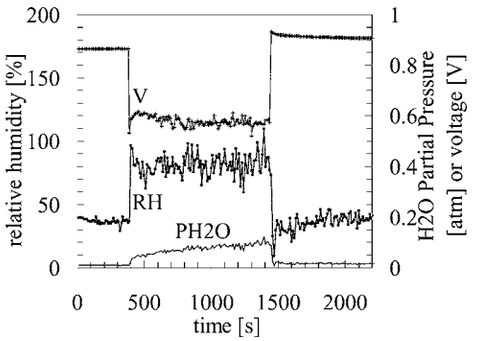

Figure 12. (a) Measurements of relative humidity, fuel cell voltage, and water vapor partial pressure as a function of time with sensor assembly located at $z = 1.6$ mm and $y = 0$ mm during a step current pulse between 0 and 333 mA/cm^2.

Figure 12 shows RH and P_{H_2O} transients measured under the same current load cycling conditions (between 0 and 333 mA/cm^2). While the RH signal shows very little transient response, the P_{H_2O} response shows a larger variation under constant current load. The initial portion of the P_{H_2O} transient may be approximated with an exponential, yielding a time constant $\tau_{H_2O} \sim 14$ s. This time constant essentially reflects the rise time of the humidity sensor, therefore an accurate measure of the time scale of the initial P_{H_2O} transient is unresolved, but we can bound its value to less than about 14 s. The subsequent time-dependent increase in P_{H_2O} is far slower and nonexponential in nature. This response is indicative of liquid water accumulation at the cathode surface as described earlier. When the current is interrupted at $t \sim 1500$ s, P_{H_2O} quickly returns to the ambient condition, again with an approximate 14 s relaxation time. (This time, however, note that the P_{H_2O} signal does not manifest a secondary, linear component.) The RH response, on the other hand, shows an interesting overshoot behavior. Most likely, this overshoot is associated with limitations in the intrinsic response time of the humidity sensor (refer to the section on humidity sensor calibration). We note, for completeness, that this overshoot may also be caused by the time lag between the immediate interruption of water production and the much slower decrease in cell temperature. As a consequence of such a lag, the still-warm air above the cathode would experience an abrupt decrease in RH, which presumably recovers as the cell (and surrounding air) cools down.

Conclusion

The data provided in this paper represent the in situ measurements of temperature and reactant species distributions above the cathode of a planar air-breathing cell. These measurements provide insight into the character of heat and mass transport in air-breathing fuel cells.

Microsensor measurements of temperature, P_{O_2}, and P_{H_2O} above the cathode surface of an air-breathing fuel cell during IV polarization reflect substantial changes in these quantities with increasing current density. A linear decrease in P_{O_2} and a linear increase in P_{H_2O} are observed with increasing current density, consistent with flux balance. A maximum of RH near the point of maximum power is consistent with a linear increase in P_{H_2O} and an exponential increase in temperature with increasing current density.

Our spatially resolved z-profile measurements indicate that thermal and reaction species effects extend up to 6 mm above the cathode surface. Complimentary y-profile measurements reveal that the cathode rib structure also visibly influences the oxygen distribution (although the ribs have little effect on the temperature profile along the y direction). Most significantly, these data show that thermal and species concentration effects are not confined to the GDL, but extend well above the fuel cell cathode surface. Because these effects extend far into the free-air region above the cathode surface, a major implication is that they can be substantially influenced by changes to the convective environment around the fuel cell. This means that structural modifications designed to enhance natural convection or provide even a small amount of forced flow (e.g., via a low power, low velocity fan) could yield significant benefits.

The spatial measurements were used to provide estimates for diffusion and/or convection mass transfer coefficients above the cathode surface. These estimates are within a factor of 2 of those predicted by free diffusion coefficients of oxygen and water in air. The convection mass transfer coefficients also agree well with our models for free-convection mass and heat transport.[19] Transient measurements reveal substantial differences in the time constants associated with oxygen, water, and heat transport. P_{O_2} above the cathode surface reacts quickly to variations in operating conditions with a single exponential time constant of approximately 6 s. In contrast, the temperature response exhibits an exponential transient, with a time constant of approximately 20 s, followed by a linear increase with time. The exponential transient is likely related to the thermal mass of the cell, and buildup of the thermal diffusion layer. The linear component of temperature rise is most likely related to cathode flooding and the subsequent increase in cell self-heating due to increased mass transfer losses. A P_{H_2O} transient recorded during current loading shows a fast initial exponential transient; but unfortunately, the time constant of this P_{H_2O} was not resolved due to limitations in intrinsic sensor response time of $\sim$14 s. We conclude also that the transient response of the sensors is not fast enough to provide accurate estimates of the mass transfer coefficients.

The significant difference between the time constants for the P_{O_2} and the thermal transients may be exploitable in decoupling mass and heat transfer effects. We hypothesize that "oxygen interrupt" experiments[24] might be employed in such an effort. Mirroring the current pulses used in a current interrupt experiment, an oxygen interrupt experiment would employ sharp pulses of forced air, oxygen, or argon delivered to the fuel cell cathode surface in order to abruptly change the oxygen concentration. The resulting transient response of the fuel cell current (in potentiostatic mode) or voltage (in galvanostatic mode) can then be recorded and analyzed. Although the convective "pulse" may also change the heat transfer characteristics in the diffusion layer, and therefore the cathode temperature, the mass and heat effects can be decoupled from one another due to their different time scales. This decoupling is also assisted by the fact that the mass transfer impact of the pulse (for example, going from $P_{O_2} = 0.21$ atm to $P_{O_2} = 1$ atm for a pure oxygen pulse or to $P_{O_2} = 0$ atm for an argon pulse) will be far greater than the thermal impact of the pulse (since the increased convection may result in only a minor temperature change). Given the opportunity, we plan a detailed investigation of this oxygen interrupt diagnostic for passive air breathing fuel cells as future work.

Finally, we also have under way modeling efforts for passive air-breathing fuel cells. These models leverage the quantitative transport data and spatial profile measurements obtained from this study to inform a reasonable, empirically based picture of transport in the air-breathing fuel cell cathode. These models will benefit from the validation data provided here and may point the way towards possible design improvement directions for planar air-breathing fuel cells.

Acknowledgments

The authors acknowledge helpful discussions with Professor John Eaton on the placement and positioning of the microsensors and their potential influence on cathode transport.

Stanford University assisted in meeting the publication costs of this article.

References

1. T. J. McIntyre, S. W. Allison, L. C. Maxey, W. P. Partridge, M. R. Cates, R. Lenarduzzi, C. L. Britton, D. Garvey, and T. K. Plant, DOE Hydrogen Program FY

2005 Progress Report No. VII.H.2 (2005).
2. R. Bellows, M. Y. Lin, M. Arif, A. K. Thompson, and D. Jacobson, *J. Electrochem. Soc.*, **146**, 1099 (1999).
3. R. Satija, D. L. Jacobson, M. Arif, and S. A. Werner, *J. Power Sources*, **129**, 238 (2004).
4. M. A. Hickner, N. P. Siegel, K. S. Chen, D. N. McBrayer, D. S. Hussey, D. L. Jacobson, and M. Arif, *J. Electrochem. Soc.*, **153**, A902 (2006).
5. K. W. Feindel, L. P. A. LaRocque, D. Starke, S. H. Bergens, and R. A. Wasylishen, *J. Am. Chem. Soc.*, **126**, 11436 (2004).
6. K. Teranishi, S. Tsushima, and S. Hirai, *Therm. Sci. Eng.*, **11**, 35 (2003).
7. X. G. Yang, F. Y. Zhang, A. L. Lubawy, and C. Y. Wang, *Electrochem. Solid-State Lett.*, **7**, A408 (2004).
8. K. Tüber, D. Pócza, and C. Hebling, *J. Power Sources*, **124**, 403 (2003).
9. T. Fabian, J. D. Posner, R. O'Hayre, S. W. Cha, J. K. Eaton, F. B. Prinz, and J. G. Santiago, *J. Power Sources*, **161**, 168 (2006).
10. R. O'Hayre, D. Braithwaite, W. Herman, S. J. Lee, T. Fabian, S. Cha, Y. Saito, and F. B. Prinz, *J. Power Sources*, **124**, 459 (2003).
11. A. Schmitz, M. Tranitz, S. Wagner, R. Hahn, and C. Hebling, *J. Power Sources*, **118**, 162 (2003).
12. A. Schmitz, S. Wagner, R. Hahn, H. Uzn, and C. Hebling, *J. Power Sources*, **127**, 197 (2004).
13. N. P. Revsbech, *Limnol. Oceanogr.*, **34**, 478 (1989).
14. J. K. Gundersen, N. B. Ramsing, and R. N. Glud, *Limnol. Oceanogr.*, **43**, 1932 (1998).
15. "Temperature response of Unisense oxygen microsensors," Unisense Inc. technical document: http://www.unisense.com/support/pdf/tempsens-ox.pdf
16. M. Laylor, S. Calvert, T. Taylor, W. Schulz, R. Lumsden, and E. Udd, *Proc. SPIE* (2003).
17. R. O'Hayre, S. W. Cha, W. Colella, and F. B. Prinz, *Fuel Cell Fundamentals*, Wiley, New York (2006).
18. Z. Qi and A. Kaufman, U.S. Patent No. 6,805,983 (2004).
19. R. O'Hayre, T. Fabian, S. Litster, F. B. Prinz, and J. G. Santiago, *J. Power Sources*, **167**, 118 (2007).
20. J. J. Hwang, *J. Electrochem. Soc.*, **153**, A1584 (2006).
21. C. Ziegler, A. Schmitz, M. Tranitz, E. Fontes, and J. O. Schumacher, *J. Electrochem. Soc.*, **151**, A2028 (2004).
22. F. P. Incropera and D. P. DeWitt, *Fundamentals of Heat and Mass Transfer*, 5th ed. Wiley, New York (2002).
23. T. Fabian, R. O'Hayre, S. Litster, F. B. Prinz, and J. G. Santiago, *ECS Trans.*, **3**(1), 1125 (2006).
24. M. Noponen, T. Hottinen, T. Mennola, M. Mikkola, and P. Lund, *J. Appl. Electrochem.*, **32**, 1081 (2002).